1   **The structure of the influenza A virus genome**

2

3   Bernadeta Dadonaite[1], Egle Barilaite[1], Ervin Fodor[1], Alain Laederach[2], David L. V.

4   Bauer[1]

5

6   [1]Sir William Dunn School of Pathology, University of Oxford, South Parks Road,

7   Oxford OX1 3RE, UK

8   [2]Department of Biology, University of North Carolina, Chapel Hill, North Carolina,

9   USA

10

11

12 Influenza A viruses (IAVs) are segmented single-stranded negative sense RNA
13 viruses that constitute a major threat to human health. The IAV genome
14 consists of eight RNA segments contained in separate viral ribonucleoprotein
15 complexes (vRNPs) that are packaged together into a single virus particle[1,2] .
16 While IAVs are generally considered to have an unstructured single-stranded
17 genome, it has also been suggested that secondary RNA structures are
18 required for selective packaging of the eight vRNPs into each virus particle[3,4] .
19 Here, we employ high-throughput sequencing approaches to map both the
20 intra and intersegment RNA interactions inside influenza virions. Our data
21 demonstrate that a redundant network of RNA-RNA interactions is required
22 for vRNP packaging and virus growth. Furthermore, the data demonstrate
23 that IAVs have a much more structured genome than previously thought and
24 the redundancy of RNA interactions between the different vRNPs explains
25 how IAVs maintain the potential for reassortment between different strains,
26 while also retaining packaging selectivity. Our study establishes a framework
27 towards further work into IAV RNA structure and vRNP packaging, which will
28 lead to better models for predicting the emergence of new pandemic
29 influenza strains and will facilitate the development of antivirals specifically
30 targeting genome assembly.

31

32 Influenza A viruses cause seasonal epidemics as well as occasional pandemics. The

33 segmented nature of the IAV genome allows reassortment of viral genome

34 segments between established human influenza viruses and influenza viruses

35 harboured in the animal reservoir[5] . This can lead to emergence of novel influenza

36 strains, against which there is little pre-existing immunity in the human

37 population[6] . However, due to a lack of understanding of the molecular

38 mechanisms governing the packaging of the eight genome segments into a single

39 virion, it remains unclear which influenza virus strains have the potential to form

40 reassortants. In virions, as well as in infected cells, the RNA genome segments are

41 assembled into viral ribonucleoprotein (vRNP) complexes in which the termini of

42 the viral RNA (vRNA) associate with the viral RNA-dependent RNA polymerase

43 while the rest of the vRNA is bound by oligomeric nucleoprotein (NP)[2,7] . Although

44   cryo-EM studies revealed the overall architecture and organisation of vRNPs, the

45   resolution of currently available structures is not sufficiently high to provide

46   information about the conformation of the vRNA[8,9] . It is thought that, through

47   specific RNA-RNA interactions, exposed regions of vRNA in the vRNP mediate

48   segment-specific interactions during virion assembly, ensuring that the correct set

49   of eight vRNPs is selected[3,4] . However, the identities of these interacting regions as

50   well as the overall structure of vRNA in vRNPs are currently unknown.

51

52   To better understand the vRNA structure in the context of vRNPs, we employed

53   SHAPE-MaP (Selective 2'-Hydroxyl Acylation Analysed by Primer Extension and

54   Mutational Profiling), which probes the conformational flexibility of each vRNA

55   nucleotide both *ex virio* and *in virio* **(Extended Data Fig. 1)**[10,11] . For the *ex virio*

56   experiments, the eight vRNA segments were individually transcribed from plasmid

57   DNA using T7 RNA polymerase (ivtRNA) or "naked" vRNA was purified from

58   deproteinated influenza A/WSN/1933 (H1N1) (WSN) particles (nkvRNA). For the *in*

59   *virio* experiments, vRNA was probed in the context of vRNPs directly inside purified

60   virions **(Extended Data Fig. 1a)**.

61

62   Three biological replicates of the *in virio* SHAPE-MaP experiments resulted in highly

63   reproducible SHAPE reactivity profiles suggesting that there is an underlying

64   structure of vRNA in the context of vRNP **(Extended Data Fig. 2a)**. We found that

65   the eight different vRNPs *in virio* have unique vRNA conformations, as

66   demonstrated by the different SHAPE reactivity profiles **(Fig. 1a)**. Regions of

67   extensive low SHAPE reactivities *in virio* (where the median-SHAPE value is below

68   zero, **Fig. 1a**) indicate that the vRNA in the context of vRNPs is capable of

69   accommodating secondary RNA structures with extensive base-pairing. However,

70   comparison of *in virio* and *ex virio* SHAPE profiles shows a significant shift in the

71   distribution of SHAPE reactivities in virio, consistent with an overall more open (less

72   structured) RNA conformation **(Fig. 1b)**. In addition, the vRNA forms fewer high-

73   probability secondary RNA structures *in virio,* suggesting that the binding of NP

74   remodels and partially melts secondary structures in vRNPs **(Fig. 1c)**, in agreement

75   with early studies using enzymatic and chemical probing of naked and NP-bound

3

76   short RNAs[12]. Regions of high correlation between *ex virio* and *in virio* SHAPE

77   profiles reveal regions of vRNA which are capable of local secondary structure

78   formation even when NP is bound. Our data also recapitulate the RNA structures

79   that have been identified previously using computational methods[13,14] **(Fig. 1d-e;**

80   **Extended Data Fig. 2b; Extended Data Fig. 3-4)**.

81

82   The finding that secondary RNA structures are accommodated in vRNPs suggests

83   that NP is not distributed on the vRNA uniformly, in agreement with a recent study

84   of NP association with vRNA[15] . This raises the possibility that parts of the vRNA

85   could be exposed and accessible to form intermolecular RNA-RNA interactions.

86   Indeed, it has been previously proposed that the specific packaging of the eight

87   different vRNPs into the budding virus is mediated by selective RNA-RNA

88   interactions forming between the vRNPs[16-21] . We therefore proceeded to analyse

89   the intermolecular RNA interactions occurring *in virio* using SPLASH (Sequencing of

90   Psoralen Crosslinked, Ligated, and Selected Hybrids)[22] . SPLASH uses a reversible

91   intercalating reagent, psoralen, which crosslinks base-paired RNAs and allows

92   mapping and identification of crosslinked regions using high-throughput

93   sequencing. We preformed two biological replicates of SPLASH analysis using

94   purified virions and focussed our analysis on the most prevalent RNA interactions

95   found in both experiments **(Extended Data Fig. 5)**. 84% of interactions were

96   observed in both replicates.

97

98   Our analysis shows that the distribution of intermolecular interaction sites varies

99   between the eight different vRNA segments and interactions sites are not

100   restricted to certain regions, e.g. vRNA termini **(Fig. 2a)**. Most segments can

101   interact with multiple other segments and in some cases the same region can

102   mediate interactions with multiple segments. While it is unlikely that the same

103   region would interact with multiple other segments in the same virion, this finding

104   suggests that certain loci in the vRNA are more likely to be involved in

105   intermolecular RNA base-pairing than others. These data also suggest that there is

106   a level of redundancy in the intermolecular interactions, allowing multiple RNA

107   conformations to be packaged *in virio*. Notably, when we used an intermolecular

4

108 RNA interaction algorithm to compute the intermolecular free energy of the RNA-

109 RNA interaction sites identified by SPLASH, we saw a significant enrichment in low

110 energy (highly favourable interactions) compared to random permutations of the

111 same interaction dataset **(Fig. 2b-c)**. Furthermore, SHAPE-informed intramolecular

112 RNA interaction prediction shows that the identified interactions are compatible

113 with the *in virio* SHAPE reactivity profiles we have determined previously and

114 indicates that the low free energy of the interactions is maintained **(Extended**

115 **Data Fig. 6)**.

116

117 Previous studies suggested that the eight vRNA segments are assembled in a

118 hierarchal manner, with some segments being more critical than others[1] .

119 Specifically, it was found that the NA and NS segments are the most easily

120 exchangeable between viral strains, suggesting that they make the least

121 contribution to the hierarchal assembly of the eight vRNPs[23-25] . In agreement, we

122 observe that NA and NS segments form the fewest interactions with other

123 segments. Surprisingly, we also identify very few interactions between the NA and

124 HA segments (0.13% of the mapped reads), suggesting that influenza viruses

125 maintain the greatest possible antigenic diversity by limiting the interactions

126 between these two segments during genome packaging.

127

128 The sequence of the IAV genome undergoes changes as a result of the antigenic

129 drift and shift[5] . Given that the intermolecular RNA interactions we have identified

130 may be important for reassortment between the different IAV strains, we

131 questioned whether the same interactions could occur in other IAV strains as well.

132 We selected a set of IAV strains representing the pandemic strains of the last

133 century (A/Brevig Mission/1/1918 (H1N1), A/Singapore/1/57 (H2N2), A/Hong

134 Kong/1/68 (H3N2), and A/England/195/2009(H1N1)), and analyzed their potential

135 to form intermolecular RNA-RNA interactions in the same regions we identified in

136 WSN. Though not all of the interactions can form in the different strains, the

137 regions corresponding to those we identified in WSN are more likely to be involved

138 in the intermolecular base-pairing than permutated datasets (**Fig. 3a**), and a

139   number of extensive interactions are maintained in the different viral strains (**Fig.**
140   **3b**).

141

142   To address the biological role of the identified *in virio* RNA-RNA interactions we
143   used synonymous mutagenesis to disrupt RNA interactions while preserving the
144   encoded amino acid sequence. We find that mutant viruses with decreased
145   strength of intermolecular RNA-RNA interactions have significant differences in the
146   ratios of the different segments packaged into the virions compared to both the
147   wild type virus and to a control virus with mutations which do not interfere with
148   identified intermolecular RNA-RNA interactions (**Fig. 4a**). In addition, weakening of
149   intermolecular RNA-RNA interactions leads to the production of defective viral
150   particles and changes in the kinetics of virus growth (**Fig. 4b-c**).

151

152   Overall, we present the first global map of the IAV genome structure *in virio*. We
153   show that the IAV genome contains both intramolecular and intermolecular RNA
154   structures. Importantly, our study shows that *in virio,* IAV maintains an extensive set
155   of RNA-mediated interactions between vRNPs, which is important for the
156   packaging of the viral genome. Maintaining a redundant inter-vRNP interaction
157   network to facilitate the selective packaging of the different genomic segments (*vs.*
158   a limited set of interactions), could be a strategy to balance the need for selective
159   packaging with the ability to allow reassortment to occur. Our analysis suggests
160   that some, though not all, of the identified intermolecular interactions are present
161   in evolutionarily distant IAVs. A redundant inter-vRNP interaction network could
162   allow multiple pathways towards assembling the full set of eight vRNPs; having
163   multiple pathways is potentially important for the emergence of novel influenza
164   virus strains through reassortment of genome segments of two evolutionarily
165   distant viruses.

166

167   This evolutionary flexibility of genome assembly is also apparent in the location of
168   specific intermolecular RNA-RNA interaction regions. A number of these overlap
169   with regions of the genome that are evolutionarily less constrained with respect to
170   their protein-coding capacity. For example, highly prevalent interactions of the NA

6

171 and NS segments fall into regions encoding the NA stalk and the linker between

172 the N-terminal RNA-binding domain and the C-terminal effector domain of NS1,

173 respectively (**Extended Data Fig. 7**). Furthermore, a prominent interaction hotspot

174 in the PA segment, involved in interactions with multiple other segments, lies

175 immediately downstream of the overlapping PA-X open reading frame (ORF) in a

176 region that encodes the linker between the N-terminal endonuclease and C-

177 terminal domain of PA. These observations suggest that the positioning of some of

178 the intersegment RNA interaction sites may be constrained by the balance

179 between the constantly drifting RNA sequences and maintenance of the encoded

180 amino acids.

181

182 In virions, the vRNPs are organized in a "7+1" pattern with seven segments of

183 different lengths surrounding a central segment[17,26-28]. This model has led to the

184 suggestion that the central segment may act as a 'master segment' mediating the

185 selection of the other segments. We note that our analysis shows that the PA

186 segment is capable of forming multiple strong intermolecular interactions, with

187 the 5' end and the 1400-1500 nt region involved in multiple redundant interactions

188 with many other segments.

189

190 We anticipate that further studies of IAV genome structure and RNA-RNA

191 interaction networks will lead to an improved ability to predict the potential for

192 reassortment between different IAV strains and consequently will facilitate the

193 prediction of the emergence of new pandemic influenza strains. Furthermore, such

194 studies may guide the design of new antivirals targeting the assembly of the eight

195 vRNPs and blocking virus packaging.

196

197

202   Research Fellowship (to D.L.V.B.). This work was also supported by the U.S. National

203   Institutes of Health [grant numbers HL111527, GM101237 and HG008133].

204

205   **Contributions:** B.D. Designed and preformed the experiments, analysed the data

206   and wrote the paper; E.B. made mutated viruses. E.F. supervised virus work and

207   edited the manuscript; A.L. supervised SHAPE data analysis and RNA modelling.

208   D.V.L.B. designed SPLASH experiments, analysed data, supervised sequencing work

209   and edited the manuscript.

210

211   **Author Information:** Sequencing data have been deposited to Sequence Read

212   Archive (accession SRP127020 & SRP126994) and the processed SHAPE reactivities

213   and SPLASH data are available in SNRNASM format as a **supplemental table 1**. The

214   authors declare no competing financial interests. Correspondence and requests for

215   materials should be addressed to E.F. (ervin.fodor@path.ox.ac.uk) and D.L.V.B.

216   (david.bauer@path.ox.ac.uk).

217

218

Methods

Cell culture, virus growth and purification.

Madin-Darby Bovine Kidney (MDBK) epithelial cells were grown in Minimum Essential Medium (MEM; Merck), supplemented with 2 mM L-glutamine and 10% fetal calf serum. Human embryonic kidney 293T (HEK 293T) cells were maintained in Dulbecco's Modified Eagle Medium (DMEM; Merck). Viral stocks were produced by infecting MDBK cells with influenza A/WSN/33 (WSN) (H1N1) virus at an MOI of 0.001. Virus was harvested 2 days post infection. Virus stocks were purified by ultracentrifugation: firstly, the infected cell culture medium was clarified by centrifugation at 4000 rpm for 10 min at 4°C followed by centrifugation at 10,000 rpm for 15 min at 4°C. The virus was then purified by centrifugation through a 30% sucrose cushion at 25,000 rpm for 90 min at 4°C in a SW32 rotor (Beckman Coulter). The purified virus pellet was resuspended in a resuspension buffer (0.01 M Tris-HCl (pH 7.4), 0.1 M NaCl, 0.0001 M EDTA). Viruses containing synonymous mutations were produced using the 12-plasmid rescue system as described previously[29] . The primers used to generate mutations are provided in **Extended Data Table 1**. Virus growth curves were generated by infecting a 70% confluent MDBK cell layer with viral stocks at an MOI of 0.001. Supernatant from infected cells was collected at 24, 48 and 72 h post infection. The infectious virus titres were determined by plaque assay. The significance of the differences between mutated and wild type virus growth kinetics was assessed using ANOVA with Dunnett's Multiple Comparison Test on GraphPad Prism software. Haemagglutination assays were carried out by serially-diluting the supernatants from infected cells in phosphate-buffered saline (PBS) in a 96-well plate. An equal volume of 0.5% chicken blood was added to the serial dilutions and the plates were incubated at 4°C until hemagglutination was observed.

Selective 2′-hydroxyl acylation analysed by primer extension and mutational profiling (SHAPE-MaP)

1-methyl-7-nitroisatoic anhydride (1M7) was custom synthesised from 4-nitroisatoic anhydride as described previously[30] . For the ivtRNA experiments each vRNA segment was synthesised from a linear DNA template using the HiScribe™ T7

251   High Yield RNA Synthesis Kit (NEB). The products were checked for size and purity

252   on a 3.5% PAGE-urea gel. nkvRNA samples were prepared by purifying the WSN

253   particles over sucrose cushion as described above. Purified viruses were treated

254   with 250 µg/mL of Proteinase K (Roche) in PK buffer (10 mM Tris-HCl (pH 7.0), 100

255   mM NaCl, 1 mM EDTA, 0.5% SDS) for 40 min at 37°C. Before the modification

256   ivtRNA and nkvRNA samples were folded at 37°C for 30 min in folding buffer (100

257   mM Hepes-NaOH (pH 8.0), 100 mM NaCl, 10 mM $MgCl_2$). 1M7 (dissolved in

258   anhydrous DMSO (Merck)) was added to a final concentration of 10 mM to the

259   folded RNA and the samples were incubated for 75 s at 37°C. The *in virio*

260   modifications were performed by adding 1M7 directly to the purified virus stocks.

261   The ability of SHAPE reagents to penetrate viral particles was initially tested as

262   described previously [31] by preforming ^{32}P-labelled primer extensions on RNA

263   extracted from SHAPE reagent-treated viral stocks using an NA segment targeting

264   primer (5'-AATTGGTTCCAAAGGAGACG-3'). In parallel to the 1M7-treated samples,

265   control samples were treated with DMSO. RNA extracted from purified viral

266   particles or denatured T7 RNA polymerase transcribed RNA was used for denatured

267   controls (DC). To prepare DC samples the RNA was mixed in DC buffer (50 mM

268   Hepes-NaOH (pH 8.0), 4 mM EDTA) with 55 % formamide and incubated at 95°C for

269   1 min. 1M7 was then added to 10 µM and the samples were incubated at 95°C for

270   an additional 1 min. N-methylisatoic anhydride (NMIA, Thermo Fisher) SHAPE

271   reagent was also tested *in virio.* Experiments with NMIA were preformed as

272   described above for 1M7, except the purified virions were treated with NMIA for 45

273   min.

274

275   Sequencing library preparation was done as described previously[11] following the

276   randomer workflow. In brief, after 1M7 or control treatments, RNA was cleaned up

277   using the RNA Clean & Concentrator™-5 kit (Zymo Research). The RNA was reverse

278   transcribed using Random Primer Mix (NEB) with Superscript II in MaP buffer (50

279   mM Tris-HCl (pH 8.0), 75 mM KCl, 6 mM $MnCl_2$, 10 mM DTT and 0.5 mM dNTPs).

280   Nextera XT DNA Library Prep Kit (Illumina) was used to prepare the DNA libraries.

281   Final PCR amplification products were size selected using Agencourt AMPure XP

282   beads (Beckman Coulter) and quality assessed using the Agilent DNA 1000 kit on a

10

283   Bioanalyser 2100 instrument (Agilent). The libraries were sequenced (2x150bp) on

284   a HiSeq4000 instrument (Illumina).

285

Sequencing of psoralen crosslinked, ligated, and selected hybrids (SPLASH)

287   SPLASH samples were prepared as published previously[22,32] with some

288   modifications. Purified virus stocks were incubated with 200 µM of EZ-Link™

289   Psoralen-PEG3-Biotin (Thermo Fisher) and 0.01% digitonin (Merck) for 5min at

290   37°C. The viruses were spread on a 6-well dish, covered with a glass plate, placed

291   on ice, and irradiated for 45 min using a UVP Ultra Violet Product™ Handheld UV

292   Lamp (Fisher). Cross-linked virus stock was treated with Proteinase K (Merck) and

293   the viral RNA (vRNA) was extracted using TRIzol (Invitrogen). An aliquot of

294   extracted vRNA was used to detect biotin incorporation using chemiluminescent

295   nucleic acid detection module kit (Thermo Fisher) on Hybond-N+ nylon membrane

296   (GE Healthcare Life Science). The rest of the extracted vRNA was fragmented using

297   NEBNext® Magnesium RNA Fragmentation Module (NEB), and size selected for

298   fragments below 200nt using RNA Clean & Concentrator™-5 (Zymo Research). The

299   samples were enriched for biotinylated vRNA using Dynabeads MyOne

300   Streptavidin C1 beads (Life Technologies) and on-bead proximity ligation and

301   psoralen crosslink reversal were carried out as published previously. Sequencing

302   libraries were prepared using adaptor ligation as described[22,32] for the first SPLASH

303   experiment, and using the commercial SMARTer smRNA-Seq Kit (Clontech) for the

304   second SPLASH experiment. Final size selection was done by running the PCR-

305   amplified sequencing libraries on a 6% PAGE gel (Thermo Thermo Fisher Fisher) in

306   TBE and selecting for 200-300bp DNA. Libraries were sequenced either 1x or

307   2x150bp on a NextSeq 500 instrument (Illumina).

308

Processing of SHAPE-MaP sequencing reads

310   The sequencing reads were trimmed to remove adaptors using Skewer[33]. The

311   SHAPE reactivity profiles were generated using the published ShapeMapper

312   pipeline[11], which aligns the reads to the reference genome using Bowtie 2 and

313   calculates mutation rates at each nucleotide position. The mutation rates are then

314   converted to the SHAPE reactivity values defined as:

11

$$R = \frac{mutr_{1M7} - mutr_{DMSO}}{mutr_{DC}}$$

315 , where $mutr_{1M7}$ is the nucleotide mutation rate in 1M7 treated sample, $mutr_{1M7}$ is

316 the mutation rate in the DMSO treated sample and $mutr_{DC}$ is the mutation rate in

317 the denatured control. All SHAPE reactivities are normalised to an approximate 0-2

318 scale by dividing the SHAPE reactivity values by the average reactivity of the 10%

319 most highly reactive nucleotides after excluding outliers (defined as nucleotides

320 with reactivity values that are greater than 1.5x the interquartile range).

321

322 **Processing of SPLASH sequencing reads**

323 The sequencing reads were first deduplicated using clumpify.sh (BBMap package;

324 https://sourceforge.net/projects/bbmap/) and adaptors were trimmed using

325 Cutadapt[34] . STAR[35] was used to align the reads to the WSN viral reference genome.

326 Only the chimeric reads in which at least 30 nucleotides aligned to the reference

327 segments were used in further processing (STAR parameter –chimSegmentMin 30).

328 CIGAR strings in each read alignment were processed to find the read start and end

329 coordinates. The reads aligning to the same partner segments and overlapping

330 positions in the first and second SPLASH experiment were combined. Overlapping

331 reads between the same partner segments in the final read set were merged and

332 expanded to cover the total read window. The start and end coordinates for all

333 interaction sites were defined as the 5' and 3' terminal positions of the expanded

334 read site. The set of interactions was visualised using Circos[36]. Final chimeric read

335 set is provided in **Supplementary table 2**.

336

337 **RNA structure predictions**

338 The IntaRNA (v2.0.4) algorithm[37] with the minimum seed requirement of 4 bp was

339 used to predict the ability of RNA-RNA interactions to occur in the regions

340 identified during the SPLASH analysis. Permutated data sets were generated by

341 randomly shuffling the specific interaction partners identified by SPLASH and

342 assessing the interaction ΔG energies using IntaRNA. The significance of the

343 difference between the probability distributions of the ΔG energies associated with

344 the SPLASH-identified intermolecular RNA interactions versus the permutated

345 datasets was calculated using Wilcox Rank-Sum Test in R software. The IntaRNA

346 structure predictions were then used to trim the interaction regions to the

347 nucleotides involved in the base-pairing. For SHAPE-informed RNA-RNA interaction

348 predictions RNAcofold from ViennaRNA package (v2.4.1) was used[38]. For

349 intramolecular RNA structure predictions RNAStructure package (v6.0) was

350 employed [39] using the *Fold* and *Partition* commands to predict secondary RNA

351 structures and partition functions for each segment, respectively. SHAPE

352 reactivities were included as pseudoenergy restraints. A 50 nt sliding median

353 window correlation analysis between the *ex virio* and *in virio* SHAPE reactivity

354 profiles was used to determine the extent of SHAPE correlation between the T7-

355 transcribed RNA and vRNP-associated RNA. We found that no correlation existed

356 >150 nt, and therefore set the maximum pairing distance constraint for structure

357 and partition function predictions to 150 nt. For the intramolecular structure

358 predictions we set the nucleotides within the promoter region to be single

359 stranded.

360

361 **RT-qPCR**

362 vRNA was extracted from rescued virus stocks using the Direct-zol™ RNA MiniPrep

363 kit (Zymo Research), including a DNase treatment step. vRNA was reverse

364 transcribed using SuperScript™ III (Thermo Fisher), per the manufacturer's

365 instructions, using an equimolar ratio of the universal vRNA primers (**Extended

366 Data Table 2**) and primer extension at 37°C for 1 h. qPCR was performed using the

367 Brilliant III Ultra-Fast Probe High ROX QPCR Master Mix (Agilent) with segment-

368 specific primers and probes (**Extended Data Table 2**).

369

13

370 **Figure legends**

371 **Figure 1** | **SHAPE-MaP analysis of the influenza A virus genome structure. a,**

372 Median SHAPE reactivities of different vRNA segments. Medians were calculated

373 over 50 nucleotide windows and plotted relative to the global median. **b,** vRNA

374 SHAPE reactivity distributions in different samples; ***P<0.0001, Wilcox Rank-Sum

375 Test. **c,** Base-pairing probability distributions in different vRNA samples; **d,**

376 Secondary RNA structure of the NS segment. Black arcs indicate the maximum

377 expected accuracy RNA structure; only the interactions associated with greater

378 than 80% base-pairing probabilities are shown. Coloured arcs indicate the base-

379 pairing probabilities. Dashed rectangle highlights the position of the hairpin

380 shown in **e**. All sequence positions are annotated as 5'- 3' in vRNA sense. nkvRNA,

381 naked viral RNA; ivtRNA, in vitro transcribed RNA; MEA, maximum expected

382 accuracy.

383

384 **Figure 2** | **Intermolecular RNA interactions in the IAV genome. a,** The most

385 common intermolecular RNA interactions identified using SPLASH. The links

386 indicate the regions involved in inter-segment base-pairing and are coloured by

387 interaction depth on a $\log_2$ scale. The top 8% of interactions are shown, which

388 account for 82% of total chimeric reads identified. **b,** Examples of the identified

389 intermolecular interaction structures. **c,** Probability distributions of the ΔG energy

390 distributions associated with the interactions identified by SPLASH versus a

391 permutated interaction dataset (n=473). ***P<0.00001, Wilcox Rank-Sum Test.

392

393 **Figure 3** | **Intermolecular RNA interactions are conserved in different IAV**

394 **strains. a,** Distribution of ΔG energies associated with the intermolecular RNA

395 interactions in different IAV strains; ***P<0.0001, Wilcox Rank-Sum Test. **b,**

396 Examples of conserved intermolecular interaction structures. $H1N1_{1918}$, A/Brevig

397 Mission/1/1918 (H1N1); H2N2, A/Singapore/1/57 (H2N2); H3N2, A/Hong Kong/1/68

398 (H3N2); pH1N1, A/England/195/2009 (H1N1).

399

400 **Figure 4 | Intermolecular RNA interactions are important for the packaging of**

401 **vRNPs. a,** RT-qPCR analysis of the vRNA inside viruses with disrupted

402 intermolecular interaction sites. For each virus an RQ value relative to the NA

403 segment was calculated and the changes compared to the wild-type virus are

404 shown. Error bars indicate standard deviation; data from three technical replicates

405 is shown. **b**, Quantification of HAU to p.f.u. ratios in mutant viruses relative to the

406 wild type. Quantification was done on the 48 and 72 h.p.i samples from the virus

407 growth analysis shown in **c**. **c,** Growth kinetics of mutant viruses. Error bars indicate

408 standard deviation; data from two biological replicates are shown. **P<0.001,

409 ***P<0.0001, ANOVA with Dunnett's Multiple Comparison Test. RQ, relative

410 quantification; p.f.u., particle forming units; h.p.i., hours post infection. Mutant

411 viruses are labelled by indicating disrupted segment interactions: HA:PA, HA:794-

412 885 PA:64-171; M:NS, M:393-422 NS:597-626; PB2:NS, PB2:437-462 NS:649-674;

413 PB2:PA, PB2:89-132 PA:1406-1447; PA:PB1, PA:1375-1400 PB1:1603-1627.

414

Extended data legends

Extended Data Figure 1 | SHAPE-MaP analysis of the IAV genome. a, Schematic showing the vRNA samples used for SHAPE-MaP analysis. **b,** Reverse transcription reaction using vRNA that was extracted from SHAPE reagent (1M7 or NMIA) or DMSO treated viral samples. ^{32}P-labelled primer targeting NA segment vRNA was used. Bands indicate the stalling of reverse transcriptase at the sites of SHAPE modifications. **c,** Schematic of SHAPE-MaP library preparation and sequencing data analysis. **d,** Mutation rates in DMSO versus 1M7 reagent treated samples. 1M7, 1-methyl-7-nitroisatoic anhydride; NMIA, N-methylisatoic anhydride; DMSO, dimethyl sulfoxide.

Extended Data Figure 2 | SHAPE reactivity variation between replicates and SHAPE reactivity correlation between different vRNA samples. a, Comparison of the median SHAPE reactivities of NS segment vRNA. Medians were calculated over 50 nucleotide windows and plotted relative to the global median. **b,** Sliding window correlation between *ex virio and in virio* vRNA samples. Pearson correlation was calculated over 50 nucleotide windows.

Extended Data Figure 3 | SHAPE-informed secondary RNA structure of the IAV polymerase segments. Black arcs indicate the maximum expected accuracy RNA structures; only the arcs associated with greater than 80% base-pairing probabilities are shown. Coloured arcs show base-pairing probabilities. Secondary structure examples of highlighted regions are shown.

Extended Data Figure 4 | SHAPE-informed secondary RNA structure of the IAV HA, NP, NA and M segments. Black arcs indicate the maximum expected accuracy RNA structures; only the arcs associated with greater than 80% base-pairing probabilities are shown. Coloured arcs show base-pairing probabilities. Secondary structure examples of highlighted regions are shown. The pseudoknot in NP is highlighted in red.

446 **Extended Data Figure 5 | SPLASH samples and sequencing. a,** Schematic

447 showing SPLASH sample preparation. **b,** Anti-biotin dot blot analysis of RNA,

448 crosslinked with biotinylated psoralen, extracted from viral particles. **c,** Schematic

449 showing the SPLASH sequencing method and bioinformatics analysis steps. **d,**

450 Chimeric reads aligned to the HA segment from two experimental replicates versus

451 total RNA input coverage. Red trace indicates sample in which T4 RNA ligase I was

452 omitted during proximity ligation (step 5 in **a**). BPSO, biotinylated psoralen; Exp.,

453 experiment.

454

455 **Extended Data Figure 6 | SHAPE-informed intermolecular RNA interactions. a,**

456 Probability distributions of the ΔG energies associated with the most common

457 interactions identified by SPLASH versus a permutated interaction dataset as

458 determined using SHAPE-informed structure prediction. **b,** Examples of

459 intermolecular secondary RNA interaction structures based on SHAPE-informed

460 structure predictions.

461

462 **Extended Data Figure 7 | Intermolecular interactions associated with**

463 **evolutionary flexible protein regions.** Schematics of polymerase acidic protein,

464 nonstructural protein 1 and neuraminidase protein. Numbers in the brackets

465 indicate protein region amino acid positions. PA, polymerase acidic protein; NS1,

466 nonstructural protein 1; NA, neuraminidase; ORF, open reading frame.

467

468 **Extended Data Table 1 | Primers used for synonymous mutagenesis of**

469 **influenza segments.**

470

471 **Extended Data Table 2 | Primers and probes used for RT-qPCR.**

472

17

473   1. Eisfeld AJ, Neumann G, Kawaoka Y. At the centre: Influenza A virus ribonucleoproteins. *Nature*

474   *Reviews Microbiology*. 2015;13(1):28-41.

475   2. te Velthuis AJ, Fodor E. Influenza virus RNA polymerase: Insights into the mechanisms of viral RNA

476   synthesis. *Nature Reviews Microbiology*. 2016;14(8):479-493.

477   3. Gerber M, Isel C, Moules V, Marquet R. Selective packaging of the influenza A genome and

478   consequences for genetic reassortment. *Trends Microbiol*. 2014;22(8):446-455.

479   4. Hutchinson EC, von Kirchbach JC, Gog JR, Digard P. Genome packaging in influenza A virus. *J Gen*

480   *Virol*. 2010;91(2):313-328.

481   5. Lowen AC. Constraints, drivers, and implications of influenza A virus reassortment. *Annual Review*

482   *of Virology*. 2017;4(1).

483   6. Taubenberger JK, Kash JC. Influenza virus evolution, host adaptation, and pandemic formation.

484   *Cell host & microbe*. 2010;7(6):440-451.

485   7. Pflug A, Lukarska M, Resa-Infante P, Reich S, Cusack S. Structural insights into RNA synthesis by

486   the influenza virus transcription-replication machine. *Virus Res*. 2017.

487   8. Arranz R, Coloma R, Chichon FJ, et al. The structure of native influenza virion ribonucleoproteins.

488   *Science*. 2012;338(6114):1634-1637. doi: 10.1126/science.1228172 [doi].

489   9. Moeller A, Kirchdoerfer RN, Potter CS, Carragher B, Wilson IA. Organization of the influenza virus

490   replication machinery. *Science*. 2012;338(6114):1631-1634. doi: 10.1126/science.1227270 [doi].

491   10. Wilkinson KA, Gorelick RJ, Vasa SM, et al. High-throughput SHAPE analysis reveals structures in

492   HIV-1 genomic RNA strongly conserved across distinct biological states. *PLoS biology*. 2008;6(4):e96.

493   11. Smola MJ, Rice GM, Busan S, Siegfried NA, Weeks KM. Selective 2 [prime]-hydroxyl acylation

494   analyzed by primer extension and mutational profiling (SHAPE-MaP) for direct, versatile and

495   accurate RNA structure analysis. *Nature protocols*. 2015;10(11):1643-1669.

496   12. Baudin F, Bach C, Cusack S, Ruigrok RW. Structure of influenza virus RNP. I. influenza virus

497   nucleoprotein melts secondary structure in panhandle RNA and exposes the bases to the solvent.

498   *EMBO J*. 1994;13(13):3158-3165.

499   13. Kobayashi Y, Dadonaite B, van Doremalen N, Suzuki Y, Barclay WS, Pybus OG. Computational

500   and molecular analysis of conserved influenza A virus RNA secondary structures involved in

501   infectious virion production. *RNA biology*. 2016;13(9):883-894.

502   14. Gultyaev AP, Tsyganov-Bodounov A, Spronken MI, Van Der Kooij S, Fouchier RA, Olsthoorn RC.

503   RNA structural constraints in the evolution of the influenza A virus genome NP segment. *RNA*

504   *biology*. 2014;11(7):942-952.

505   15. Lee N, Le Sage V, Nanni AV, Snyder DJ, Cooper VS, Lakdawala SS. Genome-wide analysis of

506   influenza viral RNA and nucleoprotein association. *Nucleic Acids Res*. 2017;45(15):8968-8977.

507   16. Gavazzi C, Yver M, Isel C, et al. A functional sequence-specific interaction between influenza A

508   virus genomic RNA segments. *Proc Natl Acad Sci U S A*. 2013;110(41):16604-16609. doi:

509   10.1073/pnas.1314419110 [doi].

510   17. Fournier E, Moules V, Essere B, et al. A supramolecular assembly formed by influenza A virus

511   genomic RNA segments. *Nucleic Acids Res*. 2011;40(5):2197-2209.

512   18. Marsh GA, Rabadan R, Levine AJ, Palese P. Highly conserved regions of influenza a virus

513   polymerase gene segments are critical for efficient viral RNA packaging. *J Virol*. 2008;82(5):2295-

514   2304. doi: JVI.02267-07 [pii].

515   19. Gog JR, Afonso EDS, Dalton RM, et al. Codon conservation in the influenza A virus genome

516   defines RNA packaging signals. *Nucleic Acids Res*. 2007;35(6):1897-1907.

517   20. Hutchinson EC, Wise HM, Kudryavtseva K, Curran MD, Digard P. Characterisation of influenza A

518   viruses with mutations in segment 5 packaging signals. *Vaccine*. 2009;27(45):6270-6275.

519   21. Hutchinson EC, Curran MD, Read EK, Gog JR, Digard P. Mutational analysis of cis-acting RNA

520   signals in segment 7 of influenza A virus. *J Virol*. 2008;82(23):11869-11879. doi: 10.1128/JVI.01634-08

521   [doi].

522   22. Aw JGA, Shen Y, Wilm A, et al. In vivo mapping of eukaryotic RNA interactomes reveals principles

523   of higher-order organization and regulation. *Mol Cell*. 2016;62(4):603-617.

524   23. Greenbaum BD, Li OT, Poon LL, Levine AJ, Rabadan R. Viral reassortment as an information

525   exchange between viral segments. *Proc Natl Acad Sci U S A*. 2012;109(9):3341-3346. doi:

526   10.1073/pnas.1113300109 [doi].

527   24. White MC, Steel J, Lowen AC. Heterologous packaging signals on segment 4, but not segment 6

528   or segment 8, limit influenza A virus reassortment. *J Virol*. 2017;91(11):10.1128/JVI.00195-17. Print

529   2017 Jun 1. doi: e00195-17 [pii].

530   25. Gao Q, Palese P. Rewiring the RNAs of influenza virus to prevent reassortment. *Proc Natl Acad Sci*

531   *U S A*. 2009;106(37):15891-15896. doi: 10.1073/pnas.0908897106 [doi].

532   26. Noda T, Sugita Y, Aoyama K, et al. Three-dimensional analysis of ribonucleoprotein complexes in

533   influenza A virus. *Nature communications*. 2012;3:639.

534   27. Noda T, Sagara H, Yen A, et al. Architecture of ribonucleoprotein complexes in influenza A virus

535   particles. *Nature*. 2006;439(7075):490-492.

536   28. Fournier E, Moules V, Essere B, et al. Interaction network linking the human H3N2 influenza A

537   virus genomic RNA segments. *Vaccine*. 2012;30(51):7359-7367.

538   29. Fodor E, Devenish L, Engelhardt OG, Palese P, Brownlee GG, Garcia-Sastre A. Rescue of influenza

539   A virus from recombinant DNA. *J Virol*. 1999;73(11):9679-9682.

540   30. Turner R, Shefer K, Ares M,Jr. Safer one-pot synthesis of the 'SHAPE' reagent 1-methyl-7-

541   nitroisatoic anhydride (1m7). *RNA*. 2013;19(12):1857-1863. doi: 10.1261/rna.042374.113 [doi].

542   31. Wilkinson KA, Merino EJ, Weeks KM. Selective 2 [prime]-hydroxyl acylation analyzed by primer

543   extension (SHAPE): Quantitative RNA structure analysis at single nucleotide resolution. *Nature*

544   *protocols*. 2006;1(3):1610-1616.

545   32. Aw JGA, Shen Y, Nagarajan N, Wan Y. Mapping RNA-RNA interactions globally using biotinylated

546   psoralen. *JoVE (Journal of Visualized Experiments)*. 2017(123):e55255-e55255.

547   33. Jiang H, Lei R, Ding S, Zhu S. Skewer: A fast and accurate adapter trimmer for next-generation

548   sequencing paired-end reads. *BMC Bioinformatics*. 2014;15(1):182.

549   34. Martin M. Cutadapt removes adapter sequences from high-throughput sequencing reads.

550   *EMBnet.journal*. 2011;17(1):pp. 10-12.

551   35. Dobin A, Davis CA, Schlesinger F, et al. STAR: Ultrafast universal RNA-seq aligner. *Bioinformatics*.

552   2013;29(1):15-21.

553   36. Krzywinski M, Schein J, Birol I, et al. Circos: An information aesthetic for comparative genomics.

554   *Genome Res*. 2009;19(9):1639-1645. doi: 10.1101/gr.092759.109 [doi].

555   37. Busch A, Richter AS, Backofen R. IntaRNA: Efficient prediction of bacterial sRNA targets

556   incorporating target site accessibility and seed regions. *Bioinformatics*. 2008;24(24):2849-2856.

557   38. Lorenz R, Bernhart SH, Zu Siederdissen CH, et al. ViennaRNA package 2.0. *Algorithms for*

558   *Molecular Biology*. 2011;6(1):26.

559   39. Reuter JS, Mathews DH. RNAstructure: Software for RNA secondary structure prediction and
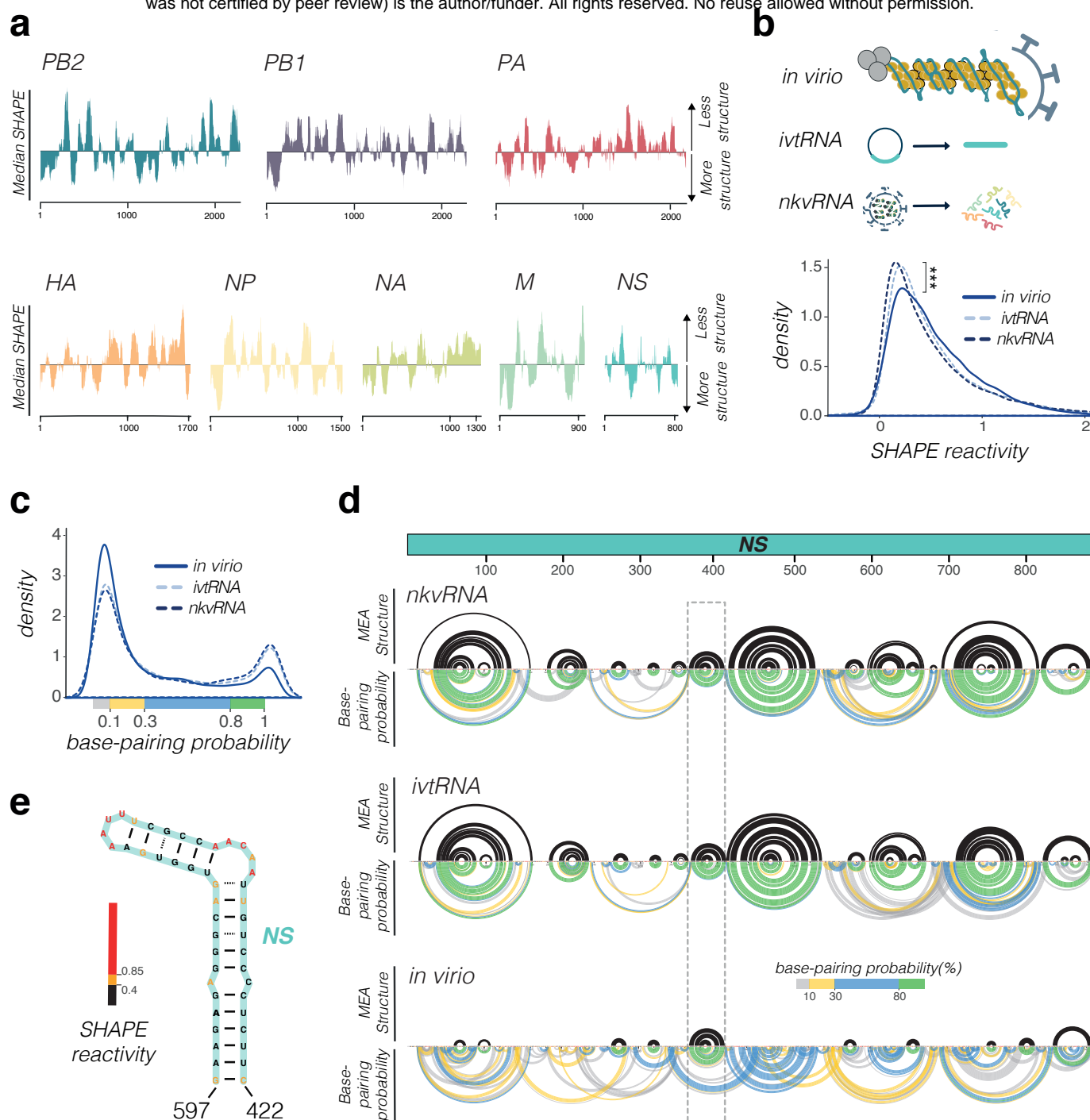
560   analysis. *BMC Bioinformatics*. 2010;11(1):1.

561

Figure 1 | SHAPE-MaP analysis of the influenza A virus genome structure. a, Median SHAPE reactivities of different vRNA segments. Medians were calculated over 50 nucleotide windows and plotted relative to the global median. **b,** vRNA SHAPE reactivity distributions in different samples; ***P<0.0001, Wilcox Rank-Sum Test. **c,** Base-pairing probability distributions in different vRNA samples; **d,** Secondary RNA structure of the NS segment. Black arcs indicate the maximum expected accuracy RNA structure; only the interactions associated with greater than 80% base-pairing probabilities are shown. Coloured arcs indicate the base-pairing probabilities. Dashed rectangle highlights the position of the hairpin shown in **e**. All sequence positions are annotated as 5′- 3′ on vRNA sense. nkvRNA, naked viral RNA; ivtRNA, in vitro transcribed RNA; MEA, maximum expected accuracy.
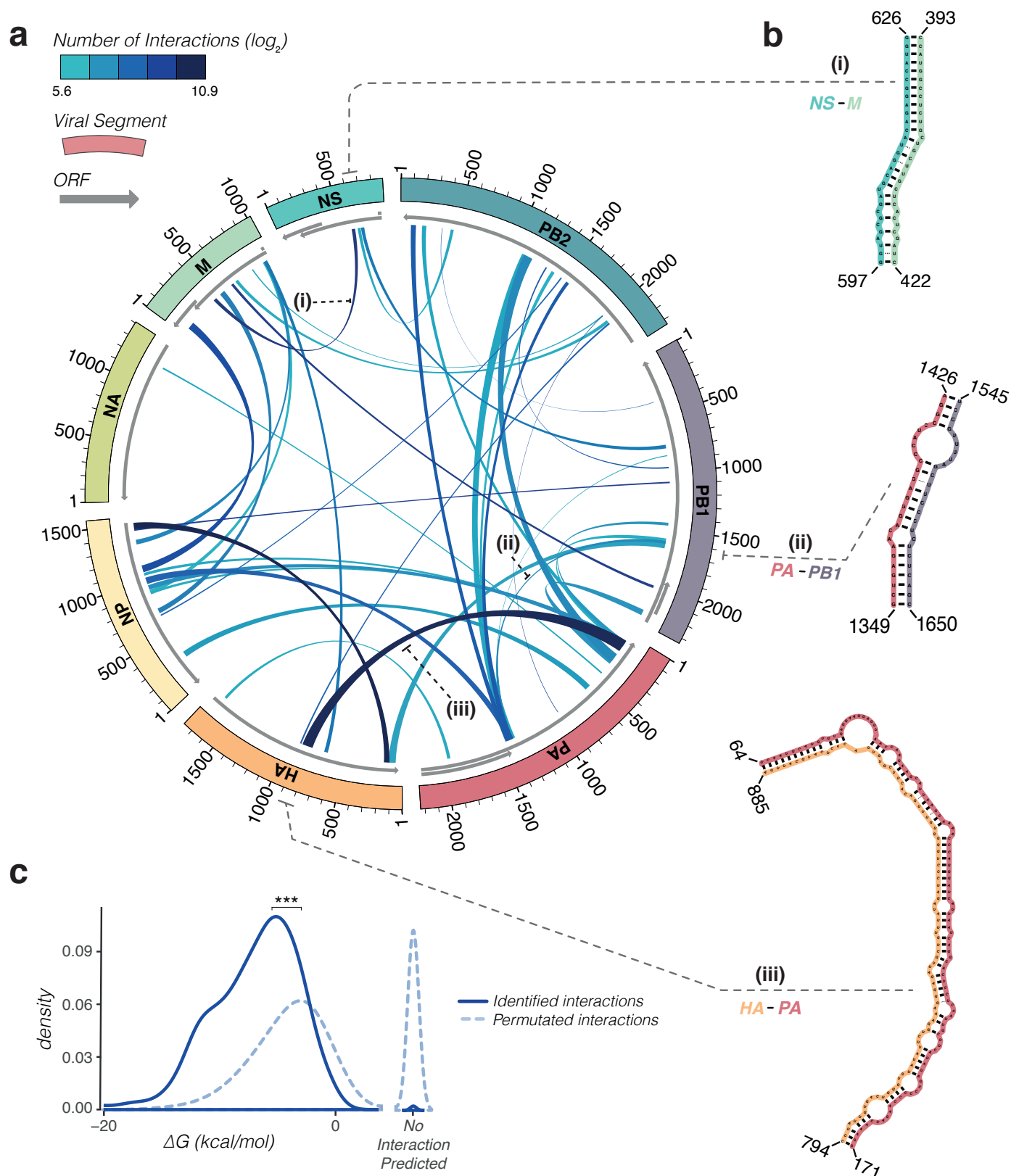
Figure 2 | Intermolecular RNA interactions in the IAV genome. a, The most common intermolecular RNA interactions identified using SPLASH. The links indicate the regions involved in inter-segment base-pairing and are coloured by interaction depth on a log2 scale. The top 8% of interactions are shown, which account for 82% of total chimeric reads identified. **b,** Examples of the identified intermolecular interaction structures. **c,** Probability distributions of the ΔG energy distributions associated with the interactions identified by SPLASH versus a permutated interaction dataset (n=473). ***P<0.00001, Wilcox Rank-Sum Test.
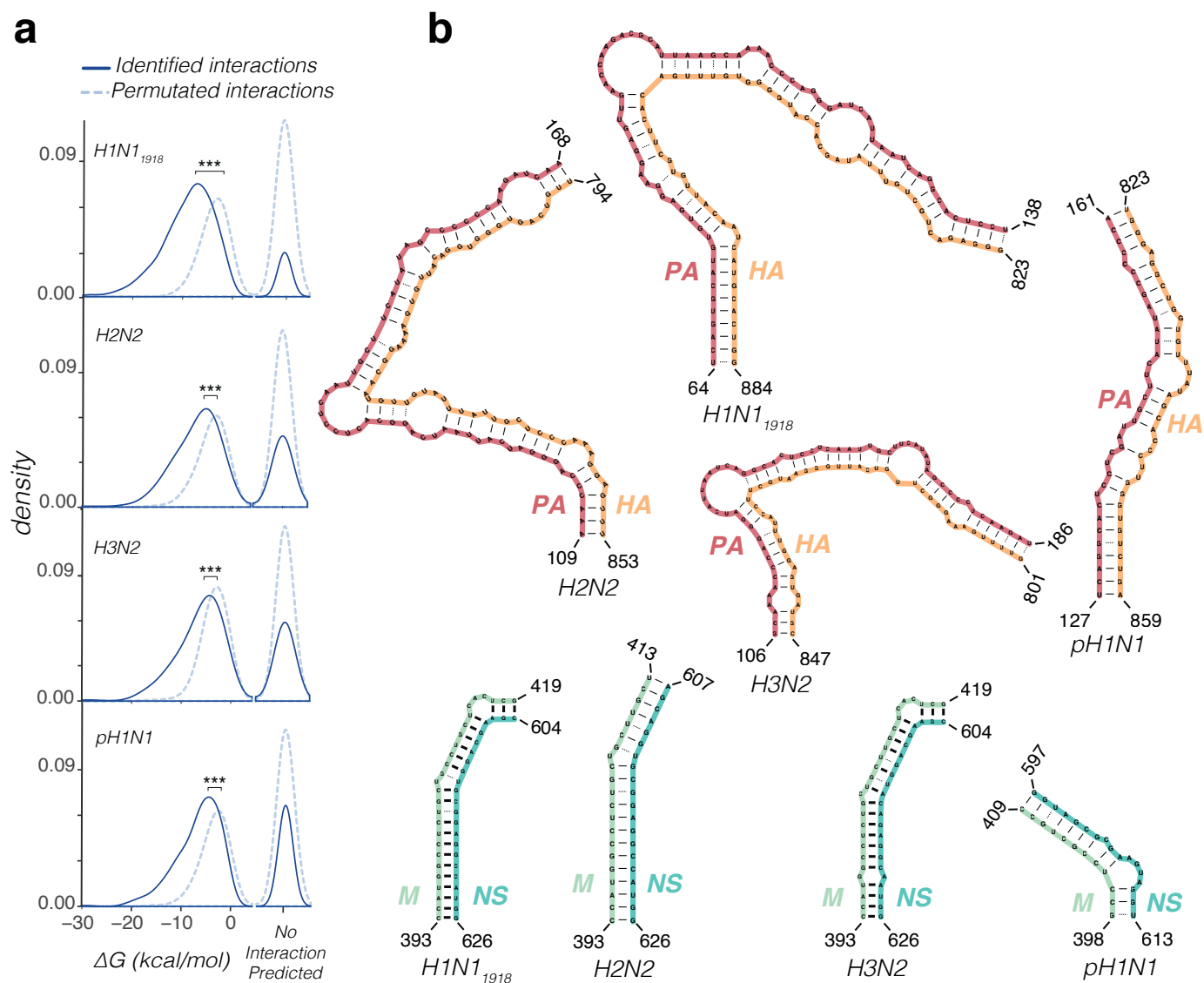
Figure 3 | Intermolecular RNA interactions are conserved in different IAV strains. a, Distribution of ΔG energies associated with the intermolecular RNA interactions in different IAV strains; ***P<0.0001, Wilcox Rank-Sum Test. **b,** Examples of conserved intermolecular interaction structures. H1N1$_{1918}$, A/Brevig Mission/1/1918 (H1N1); H2N2, A/Singapore/1/57 (H2N2); H3N2, A/Hong Kong/1/68 (H3N2); pH1N1, A/England/195/2009 (H1N1).
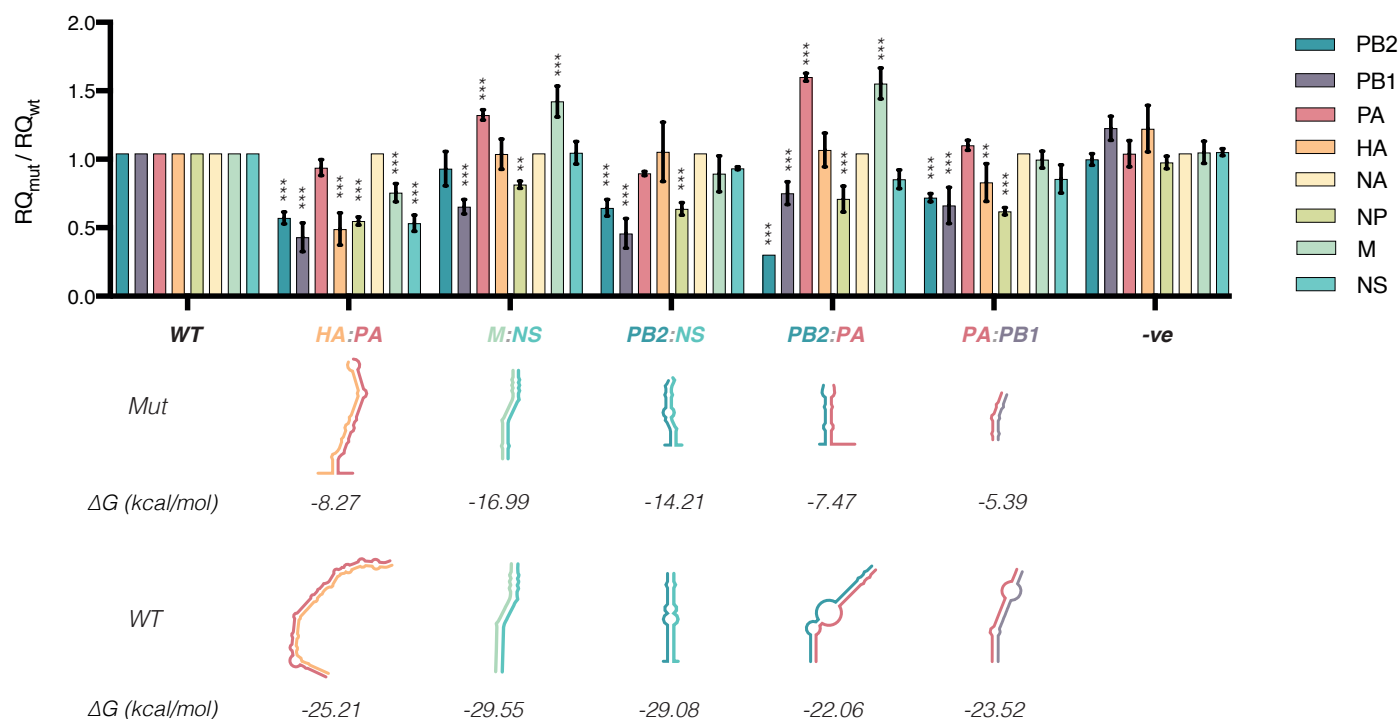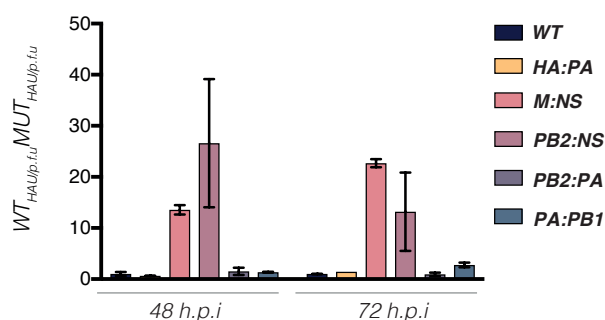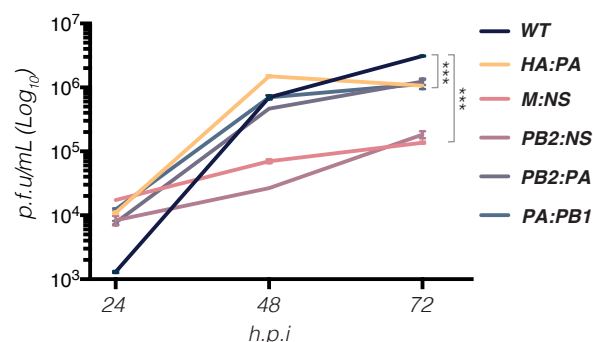
Figure 4 | Intermolecular RNA interactions are important for the packaging of vRNPs. a, RT-qPCR analysis of the vRNA inside viruses with disrupted intermolecular interaction sites. For each virus an RQ value relative to the NA segment was calculated and the changes compared to the wild-type virus are shown. Error bars indicate standard deviation; data from three technical replicates is shown. **b,** Quantification of HAU to p.f.u. ratios in mutant viruses relative to the wild type. Quantification was done on the 48 and 72 h.p.i samples from the virus growth analysis shown in c. **c,** Growth kinetics of mutant viruses. Error bars indicate standard deviation; data from two biological replicates are shown. **P<0.001, ***P<0.0001, ANOVA with Dunnett's Multiple Comparison Test. RQ, relative quantification; p.f.u., particle forming units; h.p.i., hours post infection. Mutant viruses are labelled by indicating disrupted segment interactions: HA:PA, HA:794-885 PA:64-171; M:NS, M:393-422 NS:597-626; PB2:NS, PB2:437-462 NS:649-674; PB2:PA, PB2:89-132 PA:1406-1447; PA:PB1, PA:1375-1400 PB1:1603-1627.
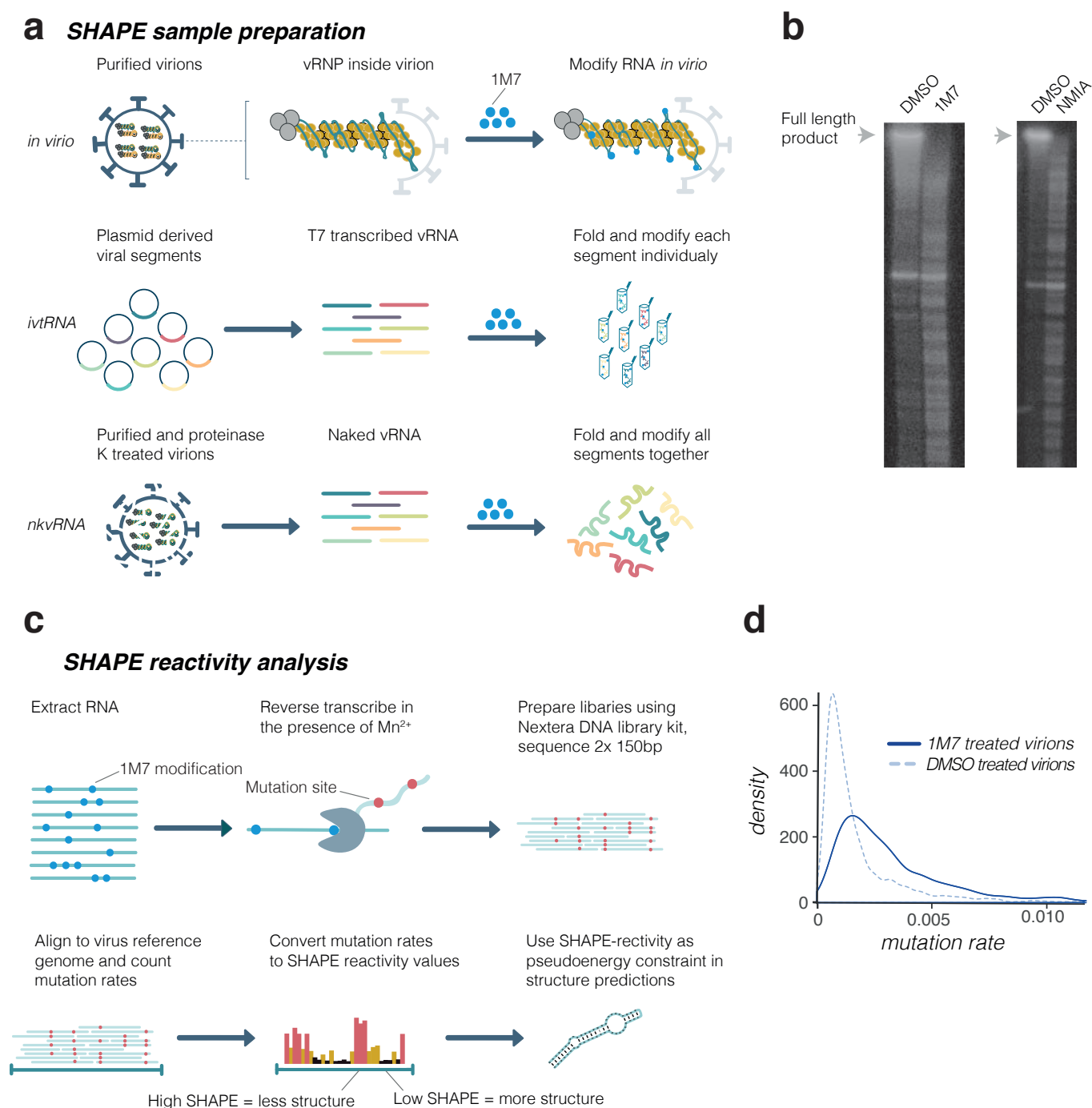
Extended figures for:
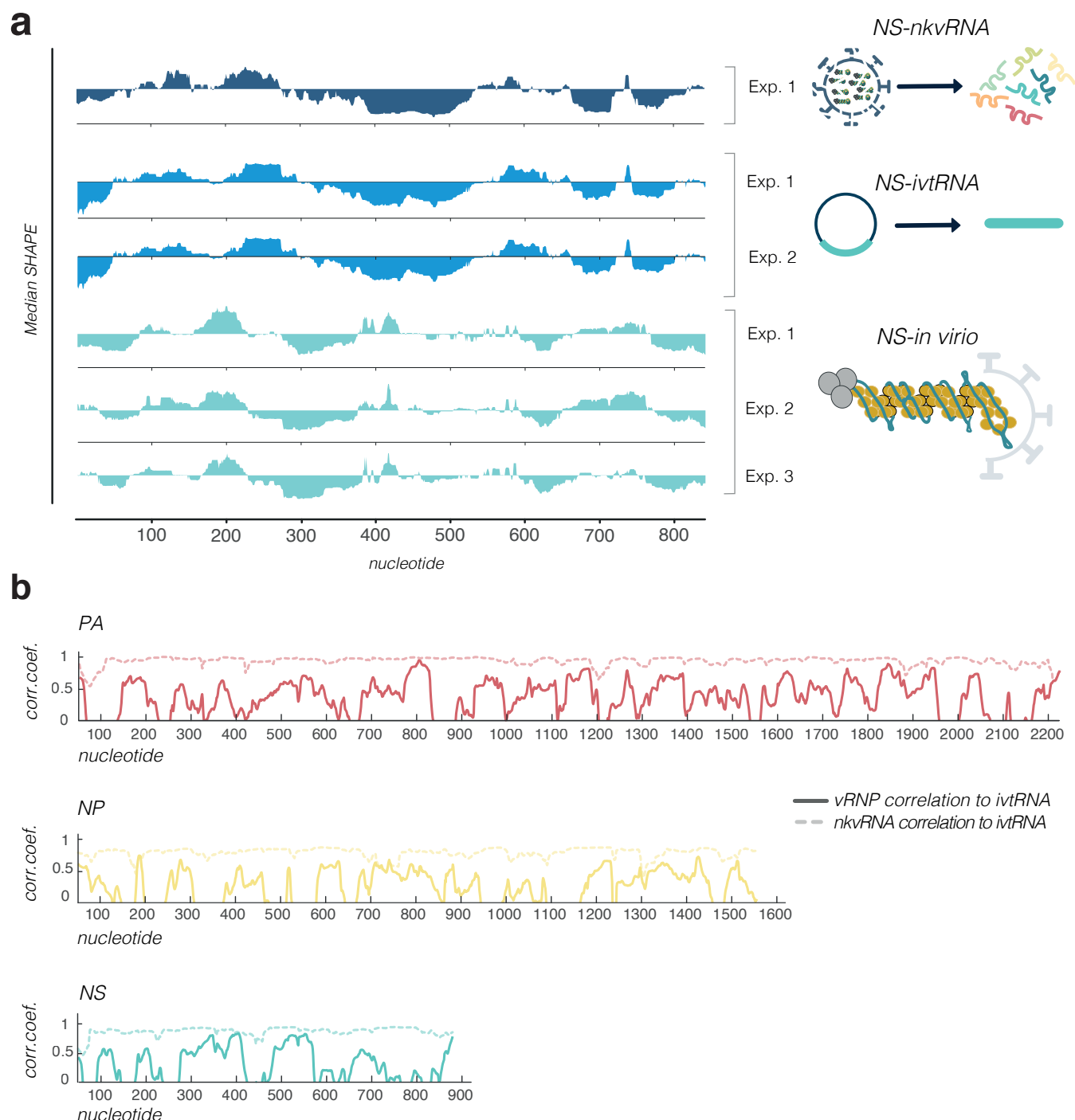
The structure of the influenza A virus genome

Bernadeta Dadonaite[1], Egle Barilaite[1], Ervin Fodor[1], Alain Laederach[2], David L. V. Bauer[1]

[1]Sir William Dunn School of Pathology, University of Oxford, South Parks Road, Oxford OX1 3RE, UK
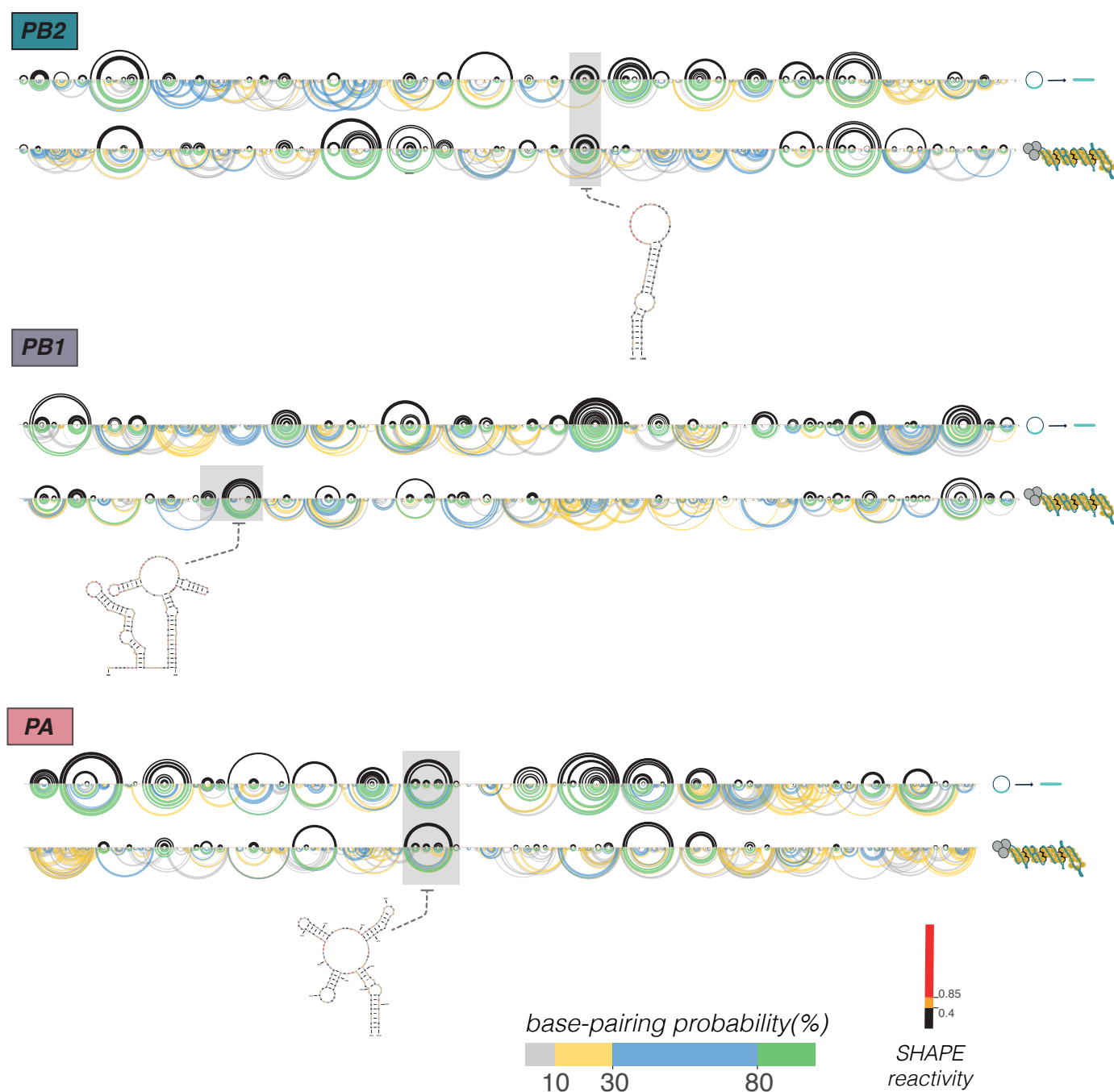
[2]Department of Biology, University of North Carolina, Chapel Hill, North Carolina, USA
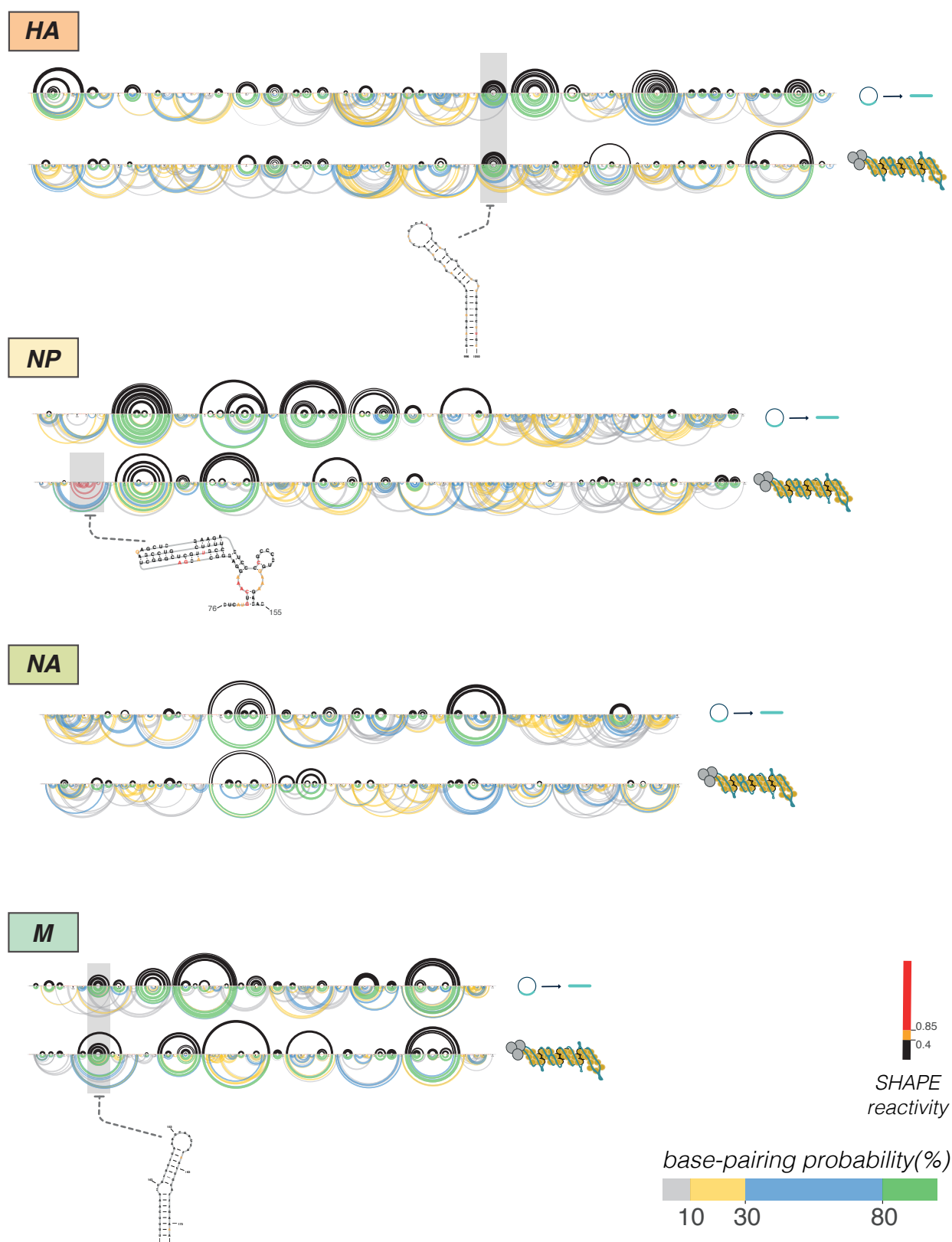
Extended Data Figure 1 | SHAPE-MaP analysis of the IAV genome. a, Schematic showing the vRNA samples used for SHAPE-MaP analysis. **b,** Reverse transcription reaction using vRNA that was extracted from SHAPE reagent (1M7 or NMIA) or DMSO treated viral samples. 32P-labelled primer targeting NA segment vRNA was used. Bands indicate the stalling of reverse transcriptase at the sites of SHAPE modifications. **c,** Schematic of SHAPE-MaP library preparation and sequencing data analysis. **d,** Mutation rates in DMSO versus 1M7 reagent treated samples. 1M7, 1-methyl-7-nitroisatoic anhydride; NMIA, N-methylisatoic anhydride; DMSO, dimethyl sulfoxide.

Extended Data Figure 2 | SHAPE reactivity variation between replicates and SHAPE reactivity correlation between different vRNA samples. a, Comparison of the median SHAPE reactivities of NS segment vRNA. Medians were calculated over 50 nucleotide windows and plotted relative to the global median. **b,** Sliding window correlation between *ex virio* and *in virio* vRNA samples. Pearson correlation was calculated over 50 nucleotide windows.
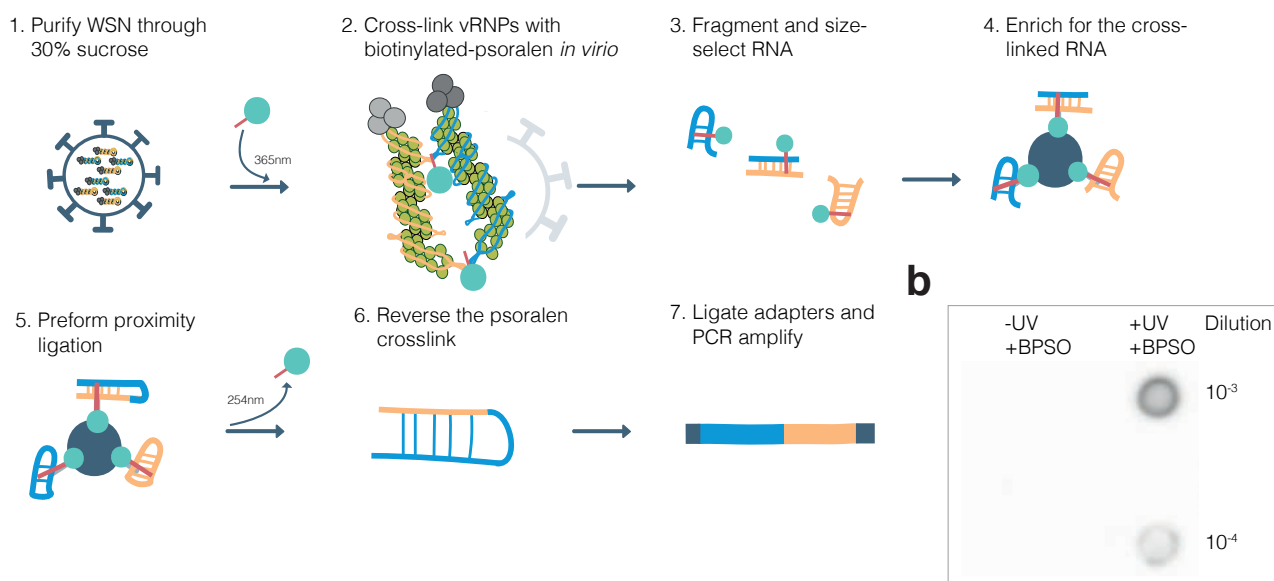
base-pairing probability(%)

10   30   80

SHAPE reactivity

0.85
0.4

Extended Data Figure 3 | SHAPE-informed secondary RNA structure of the IAV polymerase segments. Black arcs indicate the maximum expected accuracy RNA structures; only the arcs associated with greater than 80% base-pairing probabilities are shown. Coloured arcs show base-pairing probabilities. Secondary structure examples of highlighted regions are shown.

Extended Data Figure 4 | SHAPE-informed secondary RNA structure of the IAV HA, NP, NA and M segments. Black arcs indicate the maximum expected accuracy RNA structures; only the arcs associated with greater than 80% base-pairing probabilities are shown. Coloured arcs show base-pairing probabilities. Secondary structure examples of highlighted regions are shown. The pseudoknot in NP is highlighted in red.
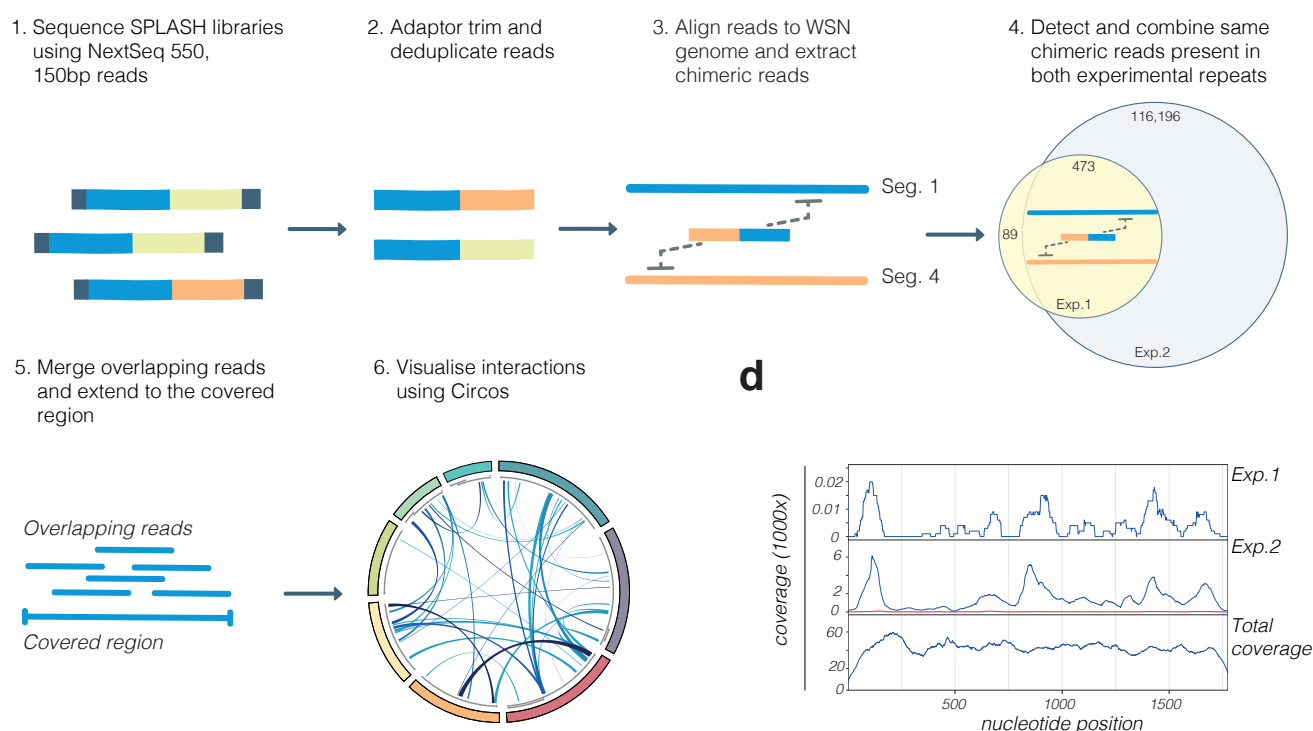
a *SPLASH sample preparation*

1. Purify WSN through 30% sucrose
2. Cross-link vRNPs with biotinylated-psoralen *in virio*
3. Fragment and size-select RNA
4. Enrich for the cross-linked RNA
5. Preform proximity ligation
6. Reverse the psoralen crosslink
7. Ligate adapters and PCR amplify

b

c *SPLASH sequencing and bioinformatics*

1. Sequence SPLASH libraries using NextSeq 550, 150bp reads
2. Adaptor trim and deduplicate reads
3. Align reads to WSN genome and extract chimeric reads
4. Detect and combine same chimeric reads present in both experimental repeats
5. Merge overlapping reads and extend to the covered region
6. Visualise interactions using Circos

d

Extended Data Figure 5 | SPLASH samples and sequencing. a, Schematic showing SPLASH sample preparation. **b,** Anti-biotin dot blot analysis of RNA, crosslinked with biotinylated psoralen, extracted from viral particles. **c,** Schematic showing the SPLASH sequencing method and bioinformatics analysis steps. **d,** Chimeric reads aligned to the HA segment from two experimental replicates versus total RNA input coverage. Red trace indicates sample in which T4 RNA ligase I was omitted during proximity ligation (step 5 in a). BPSO, biotinylated psoralen; Exp., experiment.
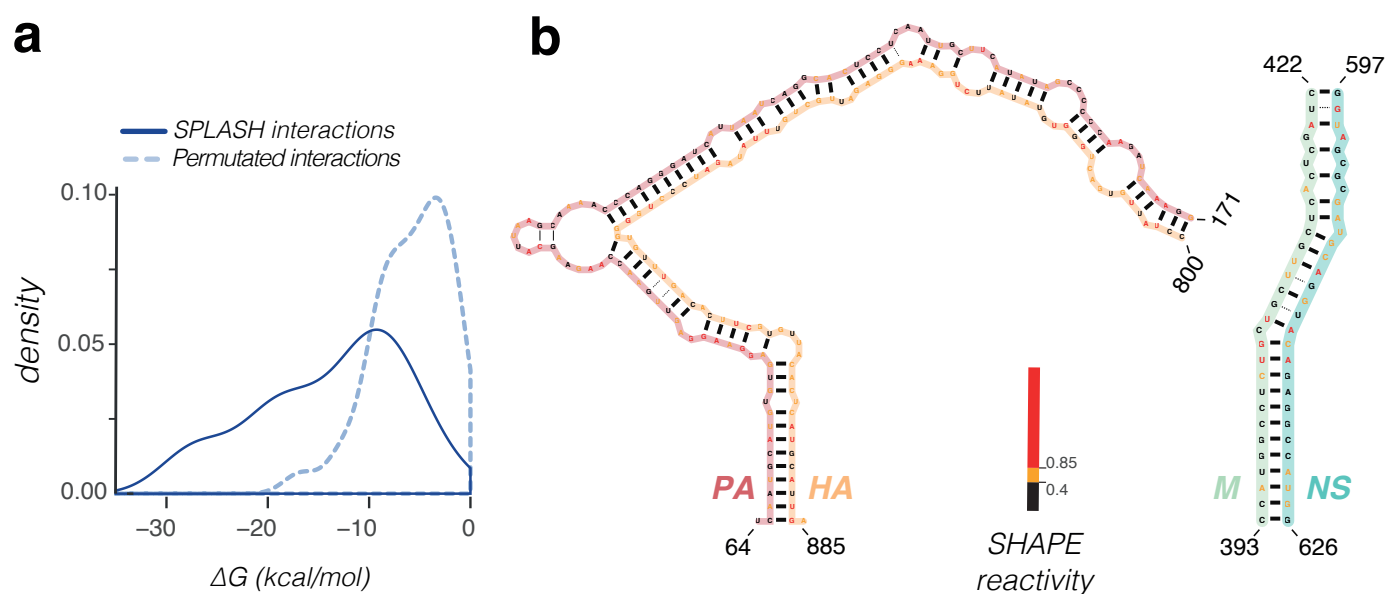
Extended Data Figure 6 | SHAPE-informed intermolecular RNA interactions. a, Probability distributions of the ΔG energies associated with the most common interactions identified by SPLASH versus a permuted interaction dataset as determined using SHAPE-informed structure prediction. **b,** Examples of intermolecular secondary RNA interaction structures based on SHAPE-informed structure predictions.
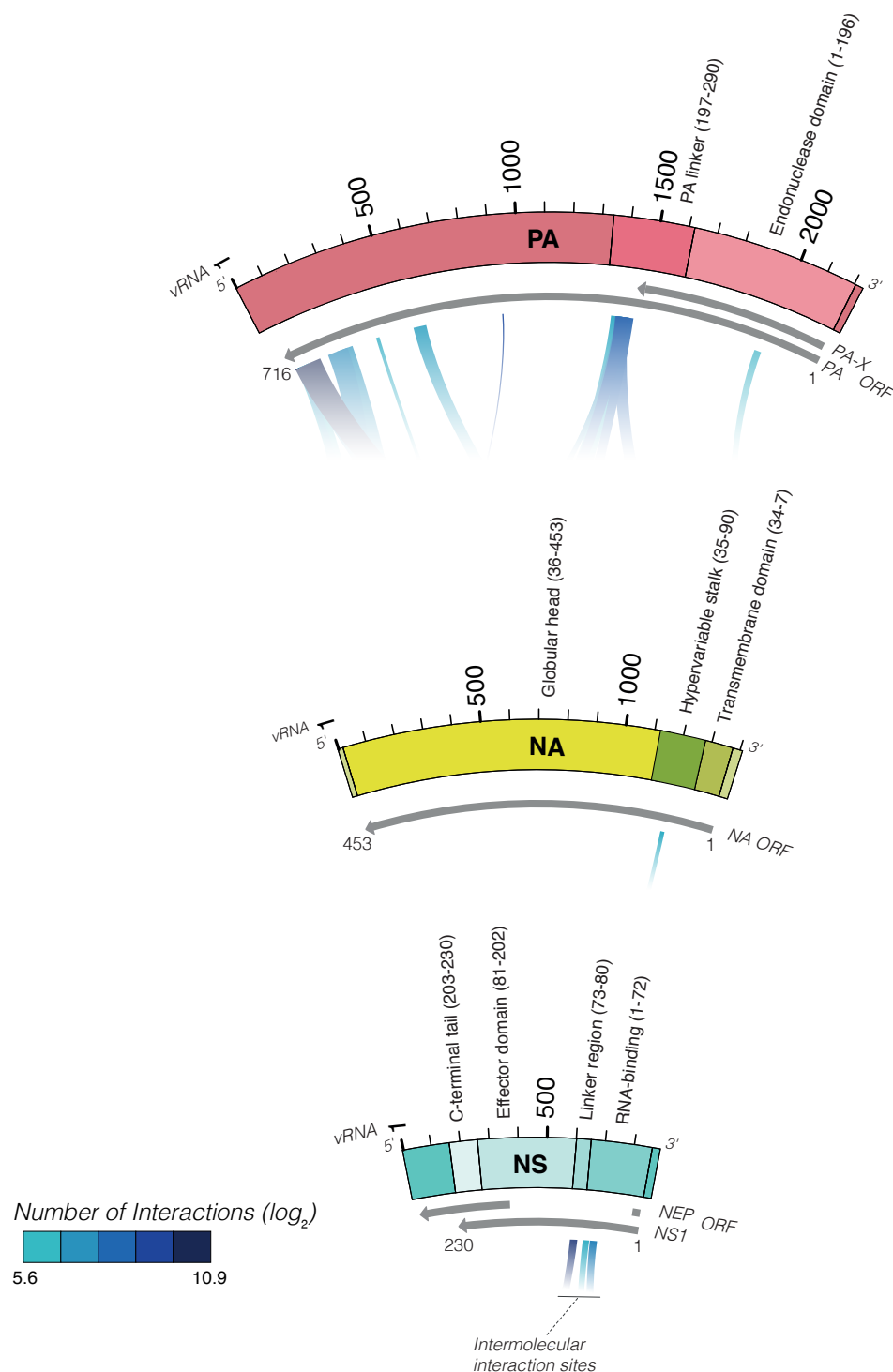
Extended Data Figure 7 | Intermolecular interactions associated with evolutionary flexible protein regions. Schematics of polymerase acidic protein, nonstructural protein 1 and neuraminidase protein. Numbers in the brackets indicate protein region amino acid positions. PA, polymerase acidic protein; NS1, nonstructural protein 1; NA, neuraminidase; ORF, open reading frame.

Extended data table 1 | Primers used for synonymous mutagenesis of influenza segments. Mutated nucleotides are shown in lower case letters.

Virus	Primers (5'-3')
HA:794-885 PA:64-171	HA_Fw GCTGTTTATAGAcCCtTGGGGTGTTTGACACTTCGTGTTACAtTCgTGCATgGACGCG HA_Rv CGCGTCcATGCAcGAaTGTAACACGAAGTGTCAAACACCCCAaGGgTCTATAAACAGC
NS:597-626 M:393-422	M_Fw CTAGCAATATCCATcGCtTCaGCTGCTTGCTCACTCGATCCAGC M_Rv GCTGGATCGAGTGAGCAAGCAGCtGAaGCgATGGATATTGCTAG
PB2:437-462 NS:649-674	PB2_Fw CCACTTTGCTTgGGgGGtGCGGCTGCGAAtGGAAGcAGTTTTAT PB2_Rv ATAAAACTgCTTCCaTTCGCAGCCGCaCCcCCcAAGCAAAGTGG
PA:1406-1447 PB2:89-132	PB2_Fw CAGTAAGTATaCTcGAGTTCCGTTTCCGTTTCATTACtAAaACCACGTCTCC PB2_Rv GGAGACGTGGTtTTaGTAATGAAACGGAAACGGAACTCgAGtATACTTACTG
PA:1375-1400 PB1:1603-1627	PB1_Fw GCAATTGCTCTaCGTTTTAGCTTaCCTCTtTCcGCATCTTTaGTCATTGTG PB1_Rv CACAATGACtAAAGATGCgGAaAGAGGtAAGCTAAAACGtAGAGCAATTGC
-ve control (HA 996-1050)	HA_Fw GCTGCAAGGCCCAAgGTtAAgGAcCAACATGGtAGGATGAACTATTACTGG HA_Rv CCAGTAATAGTTCATCCTaCCATGTTGgTCcTTaACcTTGGGCCTTGCAGC

Extended data table 2 | Primers and probes used for RT-qPCR. Locked nucleic acid nucleotides are indicated by + sign.

Reverse transcription primers		
Universal Primer 1	vRNA_3_ga GTTCAGACGTGTGCTCTTCCGATCTAGCG+AAAGCAGG	
Universal Primer 2	vRNA_3_aa GTTCAGACGTGTGCTCTTCCGATCTAGC+A+AAAGCAGG	
qPCR primers and probes		
Segment	**PCR primers**	**TaqMan dual labelled probe**
PB2	PB2_Fw CGACTGTTCGTCTCTCCCAC PB2_Rv AGAGGTGCTTACGGGCAATC	[JOE]ACAATGGTTGGGAGAAGAGCAACAGCT[BHQ1]
PB1	PB1_Fw CACTGAACCCATTTGTCAACC PB1_Rv TGGCTTGTATTCAAGATGGATCG	[TAM]GCAGTGATAATGCCAGCACATGGTCC[BHQ2]
PA	PA_Fw TTTGGACCGCTGAGAACAGG PA_Rv GGATTCGAACCGAACGGCTAC	[6FAM]CAACACCACGACCACTTAGACTTCCGG[BHQ1]
HA	HA_Fw GTTTGGTGTTTCTACAATGTAGGACC HA_Rv CGAAGACAGACACAACGGGA	[TAM]CTGGAAGCAGTGAGTCGCA[BHQ2]
NP	NP_Fw ACCCCTCCAGAAGTTCCGAT NP_Rv GCTCACTGATGCAGGGTTCA	[6FAM]GGCCGCAGGTGCTGCAGTCA[BHQ1]
NA	NA_Fw CTGTGTATAGCCCACCCACG NS_Rv GCAACCAAGGCAGCATTACC	[JOE]TGCTGGGCAGGACTCAACTTCAGT[BHQ1]
M	M_Fw GCTCACTCGATCCAGCCATT M_Rv AAGTGGCATTTGGCCTGGTA	[6FAM]TGCTGACTCCCAGCATCGGTCTCA[BHQ1]
NS	NS_Fw TCGATGTCCAGACCGAGAGT NS_Rv GAACTAGGTGATGCCCCATTCC	[JOE]CGGCTTCGCCGAGATCAGAAGTCC[BHQ1]